Impact of Friction Stir Welding on the microstructure of ODS steel

DOI:
10.1016/j.jnucmat.2016.12.033

Document Version
Accepted author manuscript

Impact of Friction Stir Welding on the microstructure of ODS steel

H. Dawson[a,*], M. Serrano[b], S. Cater[c], N. Iqbal[c], L. Almásy[d,e], Q. Tian[e], E. Jimenez-Melero[a,f]

[a]*School of Materials, The University of Manchester, Manchester M13 9PL, UK*

[b]*Structural Materials Division, Technology Department, CIEMAT, Avda de la Complutense 40, 28040 Madrid, Spain*

[c]*Friction and Forge Processes Department, Joining Technologies Group, TWI Technology Centre, Advanced Manufacturing Park, Wallis Way, Catcliffe, Rotherham S60 5TZ, UK*

[d]*State Key Laboratory Cultivation Base for Nonmetal Composites and Functional Materials, Southwest University of Science and Technology, Mianyang 621010, China*

[e]*Wigner Research Centre for Physics, Institute for Solid State Physics and Optics, P.O. Box 49, H-1525 Budapest, Hungary*

[f]*Dalton Cumbrian Facility, The University of Manchester, Moor Row CA24 3HA, UK*

Corresponding author (*):

University of Manchester

School of Materials

Oxford Road

Manchester

M13 9PL

United Kingdom

Tel.: +447837224013

Email: huw.dawson@postgrad.manchester.ac.uk

Abstract

We have assessed the impact of the welding parameters on the nano-sized oxide dispersion and the grain size in the matrix of an ODS steel after friction stir welding. Our results, based on combined small angle neutron scattering and electron microscopy, reveal a decrease in the volume fraction of the particles smaller than 80 nm in the welds, mainly due to particle agglomeration. The increase in tool rotation speed or decrease in transverse speed leads to a higher reduction in nano-sized particle fraction, and additionally to the occurrence of particle melting. The dependence of the average grain size in the matrix on the particle volume fraction follows a Zener pinning-type relationship. This result points to the principal role that the particles have in pinning grain boundary movement, and consequently in controlling the grain size during welding.

Keywords: ODS steel, friction stir welding, small angle neutron scattering, particle size distribution, Zener pinning

1. Introduction

Oxide dispersion-strengthened (ODS) steels are currently considered as leading candidate materials for the production of thin-wall cladding tubes for Gen IV fast nuclear reactors, and also for first-wall components in magnetically-confined fusion reactors [1-3]. Their attractiveness as structural materials for future nuclear energy systems lies in their enhanced high-temperature strength and creep resistance, which allows to extend the high-temperature safe limit of reactor operation beyond the value of ~600°C characteristic of ferritic/martensitic steels [4], coupled to their high resistance to the expected neutron doses potentially beyond 100 dpa [5, 6]. ODS steels are Fe-Cr based materials that contain a high density of yttrium-based oxide particles, of only a few nm in size, embedded in the ferritic matrix [7, 8]. These particles act as effective barriers for the movement of dislocations, whereas the particle/matrix interface constitutes an effective sink for interstitial atoms (e.g. H, He) and lattice defects induced by radiation [9, 10].

These materials are produced by mechanically alloying (MA) a mixture of high-purity metal powders along with Y_2O_3 fine particles. MA is able to produce a near homogenous distribution of alloying elements and dispersion of nanoparticles [11-13]. The powders are then consolidated by either hot isostatic pressing or hot extrusion, followed by a series of cold and/or hot rolling [14-16]. However, full reactor components cannot be directly produced from MA material, therefore a successful method for ODS steel joining is required. Fusion joining techniques are generally unsuccessful since melting the alloy severely disrupts the nanoparticle dispersion to the extent that they are unlikely to remain fit for purpose in nuclear reactor. Therefore there has been a large interest in developing a solid state technique to join ODS steels.

Friction Stir Welding (FSW) has in recent years has stood out as a promising solid-state welding solution for ODS steels. Several authors have been able to successfully join ODS steels by FSW while largely preserving the dispersion of nanoparticles [17]. During FSW a rotating tool is plunged in the workpiece and advances along a pre-defined direction while welding the two metallic plates together. This is a thermo-mechanical process that produces local temperatures between 70-90% of the melting point of the material [18, 19]. The dispersed nano-scale particles present a high thermal stability during annealing up to ~1150°C [20][21], with only a relatively small coarsening at prolonged times that is attributed to the uptake of Al by the yttrium oxide particles [22-24]. However, the severe plastic deformation and complex material flow caused by the FSW rotating tool as it advances along the weld line, in combination with the relatively high heat input, can potentially cause significant changes in the local microstructure of the welded zone.

The heat input and local plasticity introduced during FSW of high-Cr ODS steels triggers a process of dynamic recrystallization within the stir zone, leaving a roughly homogeneous distribution of roughly equiaxed grains. This normally leads to a decrease in hardness and strength of the weld with respect to the base material, and to a potential strain localization phenomenon at the boundary between the stir zone and the heat-affected zone on the advancing side of the weld [25, 26]. Additionally a bcc torsional texture has been reported in the stir zone, with a predominant <111> fiber component that is characteristic of torsional deformation processes in ferritic steels [26-28]. However, the recrystallization taking place during FSW can be used to form equiaxed grains, and therefore suppress the material anisotropy introduced during prior rolling and enhance the creep resistance of the material [29].

The influence of the FSW process on the oxide particle distribution is not yet well established and even less work has been done to investigate the effect of changing welding parameters. The aim of this paper is to investigate the impact of selected weld tool traverse speeds and rotation speeds on the particle size distribution of ODS friction stir bead-on-plate welds, while using the same tool geometry, plunge force and starting ODS steel microstructure. We also aim to assess the effect of the particle evolution on the grain size, and therefore on the recrystallization phenomenon during FSW, in the ferritic matrix. The results of this study will hopefully provide guidelines for optimising the FSW process of ODS steels, minimising the detrimental effect on the particle size distribution and optimising grain size distribution in the matrix.

2. Experimental

2.1. Base Material

The chemical composition of the steel used in this study, namely MA956 ODS steel, is given in Table 1. This material is produced by Special Metals Corporation, UK, via mechanical alloying of the mixture of the corresponding metallic powders with Y_2O_3 particles, followed by a hot extrusion step at ~1000°C. The consolidated material is then hot rolled in both the transverse and longitudinal directions using a 3-high reversing mill, followed by a recrystallization annealing treatment at 1320^0C for 1h, and finally air cooling to room temperature [30-32].

2.2. Friction Stir Welding

Bead-on-plate welds were performed on nominally 5 mm thick plates, which were produced by slicing the original plate in half through its thickness. We used a polycrystalline cubic boron nitride tool with a 25 mm diameter shoulder and a 3 mm diameter pin. Five bead-on-

plate welds were performed using a 25 kN plunge force in the presence of an argon shielding gas atmosphere. Each weld corresponded to a selected combination of tool rotation and transverse speeds, see Table 2. In order to evaluate the variations in microstructure across the welds, and therefore identify representative locations for further structural characterization, we performed Vickers micro-hardness line scans on the weld cross sections, using a Struers DuraScan automatic hardness tester and a 1 kgf ($HV_{1.0}$). The indentations were made perpendicular to the welding direction, at approximately 2 mm from the top surface of the workpiece.

2.3. Structural characterization

2.3.1. Optical and electron microscopy

The specimens were mechanically ground and polished down to 1 µm with diamond suspension, and further polished with 0.025 µm silica (OP-S) suspension. The specimens prepared for optical microscopy were finally etched with a solution containing 15 vol.% HCl and 3 vol.% HNO_3. Optical micrographs of the weld cross sections were taken using a Keyence VK-X200K 3D laser scanning microscope, whereas micrographs of the particles present at the weld border were taken on a Struers DuraScan automatic hardness tester. The grain size distribution in the ferritic matrix and the few micrometre-sized oxide particles were probed by combining (1) Electron Backscatter Diffraction (EBSD) maps collected on a FEI Quanta 250 FEG-SEM, using an accelerating voltage of 20 kV and a scanning step size of 0.8 µm, (2) and Backscattered Electron (BSE) images taken on an FEI Magellan High Resolution FEG-SEM. Furthermore, the characteristics of the nanometre-sized particles were studied by Transmission Electron Microscopy (TEM) using an FEI Tecnai G20 microscope. For this purpose, 3 mm-thin foil samples were taken from both the base material and the centre of the transverse cross section of the weld. The electro-polishing was

performed using an electrolyte consisting of 95 vol.% methanol and 5 vol.% perchloric acid at a temperature of -40°C. Particle size distributions were derived from the TEM data using the ImageJ software package [33].

2.3.2 Small-angle neutron scattering

The nanometre-sized particle distribution in each of the welds and the base material was derived from the Small Angle Neutron Scattering (SANS) data collected on the *Yellow Submarine* instrument, which is installed at the cold neutron beamline of the 10 MW nuclear reactor of the Budapest Neutron Centre (BNC), Hungary. A monochromatic neutron beam with a mean wavelength of 8.1 Å was produced using a multidisk mechanical velocity selector. The SANS measurements were performed at room temperature, and under a magnetic field of 1.5 T in order to magnetically saturate the ferritic matrix in the ODS steel samples. The neutron scattering signal was recorded using a He gas-filled multi-wire detector with a 64 × 64 cm^2 active area. This detector was placed at two distances behind the sample, namely 1.1 and 5.2 m, in order to cover a total q-range of 0.008-0.3 $Å^{-1}$.

3. Results

3.1. Base material

Fig. 1 shows the microstructure of the base material in the representative TD/LD and TD/ND planes, where TD, LD and ND denote the Transverse, Longitudinal and Normal Directions of the plate. At the surface, the optical micrographs reveal the presence of relatively large "pancake" shaped grains in the TD/LD plane, with their shortest dimension lying along the normal direction. These grains are created by abnormal grain growth during the annealing treatment at 1320^0C after rolling. However, close to the centre line of the plate the microstructure is characterised by a predominantly of fine grains, 1-2 µm slightly elongated in LD (Fig. 1c). The transition between the near-surface coarse grained structure and the fine

grained structure inside the plate is characterised by a boundary region where both fine and coarse grains are present. This implies that the abnormal grain growth in the material is not complete, and the large central section of the plate retains its fine grained structure. The micrographs in Fig. 1 also reveal the presence of a number of particles distributed through the plate, typically 100 nm to 2 μm in diameter, together with a high density of nano-sized particles.

3.2. Friction stir welding

The friction stir welding process was performed with the tool being plunged from the fine grain structure at the top of the workpiece, after having sliced the original 10 mm plate in half through its thickness. Fig. 2 shows the optical micrograph of the cross section of one of the welds, together with the variation in hardness across the weld at approximately 2 mm from the upper surface of the workpiece. The darker central region in the optical micrograph of Fig. 2a corresponds to the zone where the tool has stirred the material, namely the stir zone (SZ), which presents a ~10-15% decrease in hardness as compared to the base material (BM). The region of ~4 mm in width on either side of the SZ corresponds to the heat-affected zone (HAZ). There is a noticeable asymmetry in the hardness profile across the weld. The transition between the SZ and the HAZ in the advancing side of the weld is relatively sharp, while the variation in hardness is more gradual in the retreating side. Moreover, we have also observed a build-up of micrometre-sized particles in a 30-50 μm thick region located at the boundary between the SZ and the HAZ. Defects, such as cavities and tunnelling voids, are visible towards the base of the SZ. Similar defects were observed in all of the different welds. Generally they were of similar size and location, though they were occasionally also observed on the retreating edge of the weld, close to the TMAZ-HAZ boundary.

3.2.1. Grain size distribution

Fig. 3 shows a representative example of an EBSD map of the stir zone, together with the grain size distribution and mean grain diameter in the matrix as a function of welding parameters. There is a weak texture at the centre of the weld for all the studied combinations of welding parameters. The grains in the matrix are elongated in the direction of the materials flow around the rotating tool, and they have an aspect ratio of ~2. All of the welds present a similar grain size distribution. However, we have observed systematic changes in the mean grain diameter with the welding parameters: the mean diameter increases with increasing rotation speed and/or decreasing transverse speed, i.e. with increasing heat input during welding.

3.2.2. Nano-particle size distribution

The changes in particle size distribution due to FSW were detected by measuring the SANS signal of samples taken from the base material and the welds, supported by TEM observations. The studied ODS steel can be considered as a dispersion of non-magnetic spherical (oxide) particles in a ferromagnetic (ferrite) matrix. For non-magnetic scatterers the magnetic contrast is equal to the square of the magnetic scattering length density of the ferromagnetic matrix. The scattering intensity of samples in a magnetic field is in general composed of two contributions:

$$I = I_{nuc} + I_{mag} \cdot (\sin(\alpha))^2 \quad (1)$$

where I_{nuc} and I_{mag} are the nuclear and magnetic scattering intensities respectively, and α is the angle between the magnetic field direction and scattering vector q. The magnetic scattering intensity can then be extracted from the intensity collected when the scattering

vector is perpendicular (α = 90°) and parallel (α = 0°) to the applied magnetic field, see Fig. 4a, according to:

$$I_{mag} = I(\alpha=90°) - I(\alpha=0°) \quad (2)$$

The *q*-dependence of I_{mag} in a system of polydisperse particles can be expressed as [34, 35]:

$$I(q) = \Delta\rho^2 \int_0^\infty N(R)V(R)^2F^2(qR)dR \quad (3)$$

where $\Delta\rho$ is the magnetic scattering length density of the matrix, R is the particle radius, $V(R)$ is the particle volume with radius of R, and $F(qR)$ is the form factor of spherical particle that takes the form of:

$$F(qR) = \frac{3[\sin(qR) - qR\cos(qR)]}{(qR)^3} \quad (4)$$

We have analysed the intensity as a function of the scattering vector (Fig. 4b) using a lognormal particle size distribution:

$$N(R) = \frac{N}{\sigma R\sqrt{2\pi}} \exp[-\frac{\ln(R/\mu)^2}{2\sigma^2}] \quad (5)$$

where μ is the median radius, N is the total number of particles and σ is the polydispersity parameter related to the width of the particle size distribution. The mean radius of nano-oxide particles is evaluated as $\mu\ exp(\sigma^2/2)$.

Fig. 4c shows the particle size distribution derived from the SANS data for the welds and the base material. There is a significant decrease in the volume fraction of the particles in the welds, in the size range probed by the SANS experiment. Fig. 4d shows the relationship between the welding parameters and the relative volume fraction of the nano-particles after welding. There is a clear decrease in the volume fraction of the particles with increasing

rotation speed or decreasing traverse speed. Fig. 5 shows illustrative examples of the behaviour of the particles in the welds, together with the size distribution obtained from TEM. The size distributions obtained by SANS (Fig. 4c) and TEM (Fig. 5d) are in good agreement. All the welds show an increase in mean particle diameter with respect to the base material, see Table 2. The micrographs obtained by TEM show a clear evidence of particle agglomeration in the welds. In some cases, the particle clusters may even be of a few hundreds of nanometres in size (Fig. 5a), although they normally below 100 nm diameter. Evidence of melting of the nanoparticles from TEM micrographs was relatively rare (Fig. 5c), and only observed in welds produced with the higher heat inputs.

4. Discussion

Our SANS results reveal a significant decrease in the measured volume fraction of the nano-particle dispersion in the welds as compared to the base material. There are three potential causes of this decrease: particle dissolution, agglomeration, or displacement away from the centre of the welds where the neutron beam was incident. As seen in Fig. 2a, there was a build-up of particles at the boarder of the TMAZ. At this scale only the larger sized particles, mostly titanium carbonitrides and aluminium oxides, were directly observed but it may be assumed that the nanoparticles would similarly displaced away from the centre of the welds, as previously observed by Charit et al. [36].

Fig. 5c shows that there has been at least some dissolution of the particles during FSW. As previously mentioned, it was however only observed for Welds 2 and 4 by TEM which were the two welds with the highest heat inputs due to having the lowest traverse speed and greatest rotational speed, respectively. The SANS data, Fig. 4c, shows that for Welds 3 and 5, with the lowest heat inputs, the smallest particles are largely unaffected and the mean diameter remains similar to that of the base material suggesting the temperature created by

these parameters is low enough that the amount of dissolution is low or negligible. For the other welds there is a very low number of particles with diameters below 3 nm detected by SANS, suggesting that dissolution of the smallest particles has occurred. The *q*-range covered in the SANS experiment allowed the detection of particles or agglomerates with diameters up to ~80 nm. Our TEM data showed that agglomerates could grow to at least this size limit, and occasionally reached several hundreds of nanometres. Particle agglomeration during FSW is likely to be the dominant cause for the reduced volume fraction of particles measured by SANS.

We have also detected a modest increase in the average particle size in all welds with respect to the base material, as have other studies on FSW of ODS steel [37-39]. In our study, the base material had been annealed at 1320°C for 1h prior to FSW. During this annealing stage, most of the Y_2O_3 particles would have already transformed into yttrium aluminium perovskite (YAP), which is stable at temperatures lower than ~1150°C. Thermocouple data on subsequent similar welds shows that the temperatures produced by these parameters di not exceed 1000°C. Coarsening by pick-up of Al by the Y_2O_3 particles is unlikely to be a significant contributor to the increase in mean particle diameter. Consequently, both the reduction in relative fraction and the increase in average size of the particles, as measured by SANS and complementarily by TEM, are mainly due to particle dissolution and/or agglomeration during FSW. The measured increase in particle size was more pronounced for increased rotation speed and decreased traverse speed. Higher heat inputs will cause the dissolution of a greater number of the smallest nanoparticles and will produce a greater amount of stirring which in turn would likely increase the number of particles that agglomerate. Since levels of dissolution were relatively low, and negligible in the lower heat input welds, most of the nanoparticles in the stir zone of the welds will have been retained after FSW. However, many of the nanoparticles exist as part of an agglomerate, hence the

number density of effective sites for pinning dislocations, trapping helium or acting as recombination sites for radiation-induced lattice defects will still be reduced.

The average grain size in the matrix of the welds was found to increase with increasing tool rotation speed and/or decreasing traverse speed. One potential cause of the increased grain size is the direct effect of the heat input during welding. Strain and strain rate also have a role in determining grain size in the SZ, but this is usually not as significant as the temperature of the weld. The SZ grain structure coarsens from its initial sub-micron grain size, and becomes more equiaxed in the thermal wake of the tool in a static annealing process [40]. Another study on FSW of MA956 [38] showed that the grain size of friction stir welded MA956 is stable during post weld heat treatment at 1300^0C for one hour. Given that the temperatures achieved in this work during FSW remained lower than 1000°C and that the exposure time during welding was below 1 min, the direct effect of the heat input on the matrix is unlikely to be the sole determining factor for the final grain size in MA956 after FSW. The alternative is the effect of FSW on the oxide particle size distribution, since the finely dispersed nano-particles play an effective pinning role for the movement of grain boundaries in the matrix, including following FSW [41, 42]. Fig. 6 shows the average grain size in the matrix as a function of the volume fraction of oxide particles. We have compared these experimental data with the Zener pinning limiting grain size, D_{zener}, given by [43]:

$$D_{zener} = \frac{4\bar{r}}{3f_v} \quad (6)$$

where $\bar{r}$ is the average particle radius and f_v is the volume fraction of particles in the welds (Table 2). The volume fraction of particles in the base material is reported to be 0.62 ± 0.10% [34]. The data in Fig. 6 shows a relatively good correlation between the measured average grain size and the values derived using Eq. (6). This implies that the oxide dispersion strongly influences the grain size in the matrix, by acting as pinning particles for grain boundaries.

The increase in particle size and decrease in volume fraction of particles with sizes below 80 nm, caused by the higher tool rotation speed and/or lower transverse speed, manifests in a higher interparticle spacing and a reduced role in retarding grain growth in the matrix during welding. Therefore, the observed decrease in hardness in the stir zone, as compared to the base material, is mainly due to (1) the increased average grain size with respect to the surrounding fine grained material, (2) the decrease in the number of particles in the size range below 80 nm, due to either particle agglomeration or, in the case of higher heat input during welding, due to particle melting or displacement to the boundary between the stir zone and the heat affected zone, and (3) a low dislocation density in the stir zone following continuous dynamic recrystallisation.

The presence of weld defects in the welds suggests that there was insufficient material flow during FSW to create fully consolidated welds. The relative motion of the tool means that the level of mixing is more inadequate on the retreating side of the weld, which is why weld defects were observed along the retreating side TMAZ boundary. It is very likely that all of the welds were too cold to sufficiently plasticise the material.

The insufficient material flow is likely to be the cause to the high levels of particle agglomeration observed. The low viscosity would cause the material to be subject to intense plastic deformation and large strain gradients to which agglomeration of dispersoids has been attributed previously by other authors in FSW [44]. Other studies on FSW of ODS steels, using higher heat inputs have been able to produce defect free welds while keeping the near homogeneous distribution of particles in the SZ [27]. The results suggest that a compromise of welding parameters may have to be met to maximise the effectiveness of the nanoparticles distribution of ODS steels after FSW. Welding with too low a heat input leaves the weld vulnerable to defects and agglomeration of the particles. However, using a higher heat input

can cause dissolution of the particles, which has been shown in some cases to severely alter the mean diameter and volume fraction of particles deleteriously.

5. Conclusions

We have performed a systematic study of the impact of the FSW parameters on both the nano-oxide particle distribution and the average grain size in the ferritic matrix of MA956 ODS steel. The main conclusions of this work are: (1) the relative volume fraction of nano-particles in the range of 2-80 nm, as measured by SANS, decreases in the stir zone with respect to the base material. This effect is more pronounced in the case of higher tool rotation speed and/or lower transverse speed, i.e. higher heat input during welding; (2) in all studied welds, the particles form agglomerates that can in some cases reach sizes above 100 nm. When the heat input during welding is relatively high, we have also observed particle dissolution; (3) the stir zone of all the welds consists of a largely homogenous grain structure with a nearly random texture. The average grain size in the matrix increases with decreasing volume fraction of particles with sizes below 80 nm; (4) the relationship between both structural parameters follows a Zener pinning-type relationship. This implies an effective pinning effect of the particles on the movement of grain boundaries in the matrix during welding. The majority of the oxide particles are retained after FSW, but their grain boundary pinning effect is reduced when they are forming relatively large agglomerates.

Acknowledgements

We gratefully acknowledge the financial support of the Engineering and Physical Sciences Research Council UK (EPSRC) through the Centre for Doctoral Training in Advanced Metallic Systems. We would like to thank CIEMAT in Spain for providing the base material of MA956 ODS steel, and to The Welding Institute for providing the welding tools and assistance during friction stir welding. We also thank the Budapest Neutron Centre for the

granted beam time and We also thank the Budapest Neutron Centre for the granted beam time and the European Commission under the 7th Framework Programme through the Key Action: Strengthening the European Research Area, Research Infrastructures under Grant Agreement no. 283883-NMI3-II, for support to perform the SANS experiment.

References

[1] P. Yvon, F. Carré. J. Nucl. Mater. 385 (2009) 217.

[2] J.S. Cheon, C.B. Lee, B.O. Lee, J.P. Raison, T. Mizuno, F. Delage, et al. J. Nucl. Mater. 392 (2009) 324.

[3] M.J. Gorley. Mater. Sci. Technol. 31 (2015) 975.

[4] R.L. Klueh, A.T. Nelson. J. Nucl. Mater. 371 (2007) 37.

[5] A. Chauhan, D. Litvinov, Y. de Carlan, J. Aktaa. Mater. Sci. Eng. A 658 (2016) 123.

[6] M.B. Toloczko, F.A. Garner, V.N. Voyevodin, V.V. Bryk, O.V. Borodin, V.V. Mel'nychenko et al. J. Nucl. Mater. 453 (2014) 323.

[7] A. Hirata, T. Fujita, Y.R. Wen, J.H. Schneibel, C.T. Liu, M.W. Chen. Nat. Mater. 10 (2011) 922.

[8] Y. Wu, J. Ciston, S. Kräemer, N. Bailey, G.R. Odette, P. Hosemann. Acta Mater. 111 (2016) 108.

[9] S.Y. Zhong, V. Klosek, Y. de Carlan, M.H. Mathon. J. Mater. Sci. 51 (2016) 2540.

[10] G.R. Odette, M.J. Alinger, B.D. Wirth. Annu. Rev. Mater. Res. 38 (2008) 471.

[11] http://www.msm.cam.ac.uk/phase-trans/mphil/MP4-4.pdf.

[12] C. Suryanarayana, E. Ivanov, V.V. Boldyrev. *Mater. Sci. Eng. A 304 (2001)* 151.

[13] R.E. Smallman, A.H.W. Ngan. *Physical metallurgy and advanced materials*. Butterworth-Heinemann, 2011.

[14] C.A. Williams, P. Unifantowicz, N. Baluc, G.D.W. Smith, E.A. Marquis. Acta Mater. 61 (2013) 219.

[15] T. Muroga, T. Nagasaka, H. Abe, S. Ukai, A. Kimura, et al. Fusion Eng. Des. 89 (2014) 1717.

[16] M. Dadé, J. Malaplate, J. Garnier, F. De Geuser, N. Lochet, A. Deschamps. J. Nucl. Mater. 472 (2016) 143.

[17] B.W. Baker, L.N. Brewer, JOM 66 (2014) 2442.

[18] R.S. Mishra, Z.Y. Ma. Mater. Sci. Eng. R 50 (2005) 1.

[19] R. Nandan, T. DebRoy, H.K.D.H. Bhadeshia. Prog. Mater. Sci. 53 (2008) 980.

[20] T. Okuda, M. Fujiwara. *J. Mater. Sci. Lett. 14* (1995) 1600.

[21] J.K. Tien. *Superalloys, supercomposites and superceramics*. Elsevier, 2012.

[22] P. Krautwasser, A. Czyrska-Filemonowicz, M. Widera, F. Carsughi. Mater. Sci. Eng. A 177 (1994) 199.

[23] P. Miao, G.R. Odette, T. Yamamoto, M. Alinger, D. Klingensmith. J. Nucl. Mater. 377 (2008) 59.

[24] C.L. Chen, P. Wang, G.J. Tatlock. Mater. High Temp. 26 (2009) 299.

[25] W. Han, A. Kimura, N. Tsuda, H. Serizawa, D. Chen, H. Je, et al. J. Nucl. Mater. 455 (2014) 46.

[26] J. Wang, W. Yuan, R.S. Mishra, I. Charit. J. Nucl. Mater. 432 (2013) 274.

[27] W. Han, S. Ukai, F. Wan, Y. Sato, B. Leng, H. Numata, et al. Mater. Trans. 53 (2012) 390.

[28] J. Baczynski, J.J. Jonas. Acta Mater. 44 (1996) 4273.

[29] S. Noh, R. Kasada, A. Kimura, S.H.C. Park, S. Hirano. J. Nucl. Mater. 417 (2011) 245.

[30] Engineering Data Sheet for Incoloy MA956, Special Metals Corporation, 2004.

[31] J.D. Whittenberger. Metall. Trans. A 12A (1981) 845.

[32] R.C. Klug, G. Krauss, D.K. Matlock. Metall. Mater. Trans A 27 (1996) 1945.

[33] C.A. Schneider, W.S. Rasband, K.W. Eliceiri. Nat. Methods, 9 (2012) 671.

[34] A.J. Jackson. *Introduction to Small-Angle Neutron Scattering and Neutron Reflectometry*, 2008.

[35] Z. Szaraz, G. Török, V. Kršjak, P. Hähner. J. Nucl. Mater. 435 (2013) 56.

[36] I. Charit, M. Frary, D. Butt, K.L. Murty, L. Zirker, J. Cole, et al. A Comparative Study of Welded ODS Cladding Materials for AFCI/GNEP Applications (No. DOE/ID/14925). University of Idaho, 2011.

[37] M.H. Mathon, V. Klosek, Y. De Carlan, L. Forest. J. Nucl. Mater. *386* (2009) 475.

[38] M. West, B. Jasthi, P. Hosemann, V. Sodesetti 2011. Friction stir welding of oxide dispersion strengthened alloy MA956, in *Friction Stir Welding and Processing VI, TMS 2011*, p.33-40.

[39] B.W. Baker, T.R. McNelley, L.N. Brewer. Mater. Sci. Eng. A 589 (2014) 217.

[40] P.B. Prangnell, C.P. Heason. Acta Mater. 53 (2005) 3179.

[41] C.L. Chen, G.J. Tatlock, A.R. Jones. J. Alloys Comp. 504, (2010) S460

[42] J.D. Robson, L. Campbell. *Sci. Technol. Weld. Join. 15* (2010) 171.

[43] A. Rollett, F.J. Humphreys, G.S. Rohrer, M. Hatherly *Recrystallization and related annealing phenomena*. Elsevier, 2004.

[44] J. Wang, W. Yuan, R.S. Mishra, I. Charit. J. Nucl. Mater. 442 (2013) 1.

Tables

Table 1. Chemical composition of the studied MA956 ODS steel (wt%).

Cr	Al	Y_2O_3	P	Ti	O	C	Mn	Si	Mo	Ni	Co	N	Cu	S	Fe
19.97	4.44	0.53	0.53	0.33	0.21	0.15	0.11	0.05	<0.05	0.04	0.03	0.022	0.009	0.004	bal.

Table 2. Welding parameters and characteristic parameters of the welded microstructures: mean grain diameter of the ferritic matrix, and relative volume fraction and mean diameter of the oxide nano-particles. 'BM' denotes the base material.

Weld No.	**Rotations per Minute (RPM)**	**Traverse Speed (mm/min)**	**Mean Grain Diameter (μm)**	**Relative Volume Fraction**	**Mean Diameter (nm)**
BM	-	-	-	1	10.8(1)
1	200	140	2.49(5)	0.64	16.0(1)
2	200	120	2.58(6)	0.53	18.8(1)
3	200	160	2.05(3)	0.77	10.8(1)
4	220	140	2.56(5)	0.58	17.2(1)
5	180	140	1.93(4)	0.83	11.4(1)

Figure captions

Fig. 1. (a)-(b) Optical image along the LD/TD and ND/TD planes respectively; (c)-(e) BSE images taken at the representative locations of the plate thickness denoted in (b); and (f) TEM image of the as-received plate material of MA956 ODS steel.

Fig. 2. (a) Optical image of the cross section of a representative bead-on-plate ODS steel weld; (b) micro-hardness measurements taken at approx. 2mm from the surface of the weld, as denoted by the dash line in (a).

Fig. 3. (a) EBSD map of the welds; (b) grain size distribution of the matrix of selected welds; (c) variation of the mean grain diameter with the tool rotation speed and transverse speed.

Fig. 4. (a) SANS data collected from a ODS steel weld sample placed under an external magnetic field of 1.6T; (b) intensity as a function of the scattering vector for the base material and selected welds; (c) oxide particle size distribution derived from the SANS data; (d) variation of the relative volume fraction of particles with the tool rotation speed and transverse speed.

Fig. 5. TEM images showing examples of (a)-(b) particle agglomeration and (c) melting; (d) particle size distribution obtained from the TEM images.

Fig. 6. (a) Mean grain diameter of the matrix as a function of the relative volume fraction of the oxide particles. The red line corresponds to the estimated Zener pinning limiting grain size (see text); (b) experimental value of the mean grain diameter for each of the studied welds, together with the estimate from Eq. (6).

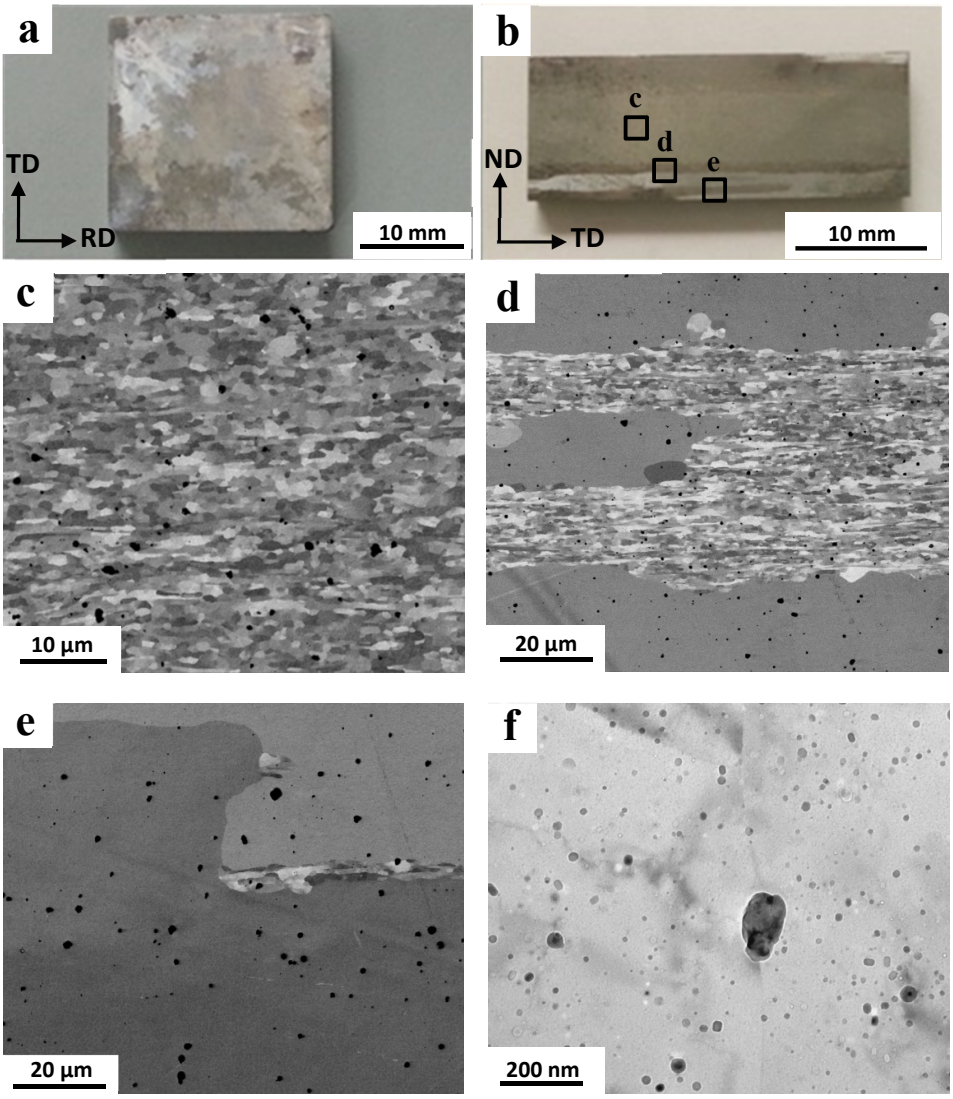

Fig. 1

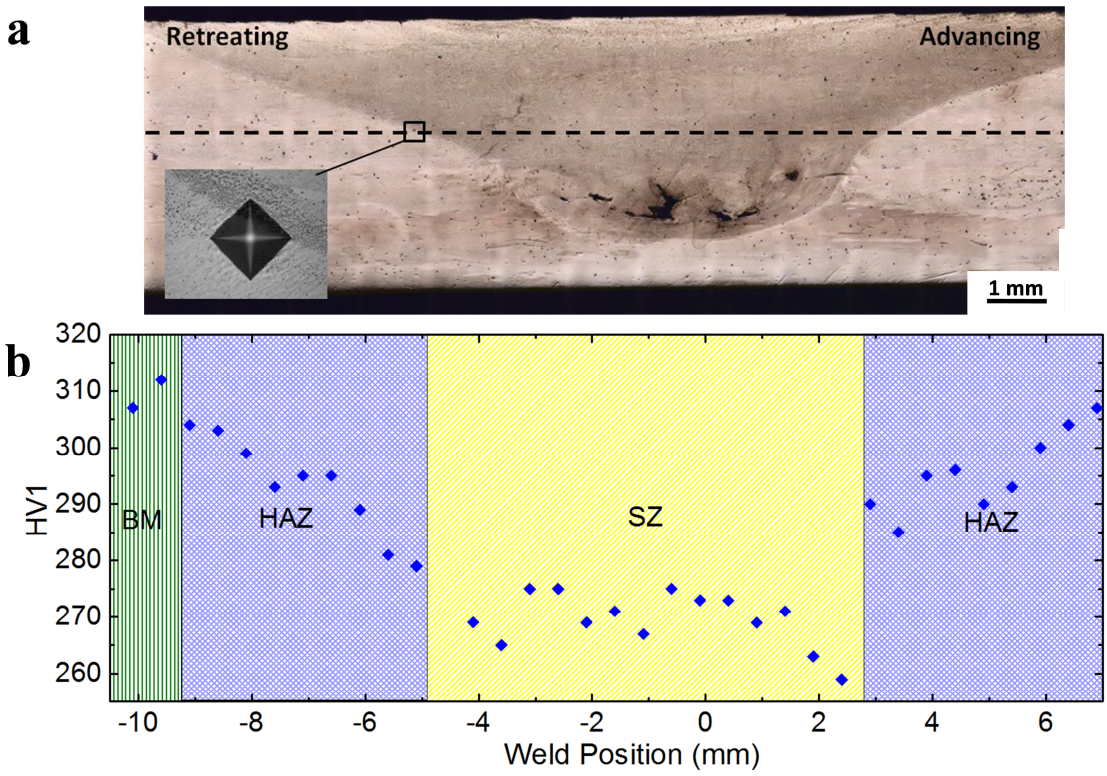
a
Retreating
Advancing
1 mm
b
HV1
320
310
300
290
280
270
260
BM
HAZ
SZ
HAZ
-10
-8
-6
-4
-2
0
2
4
6
Weld Position (mm)

Fig. 2

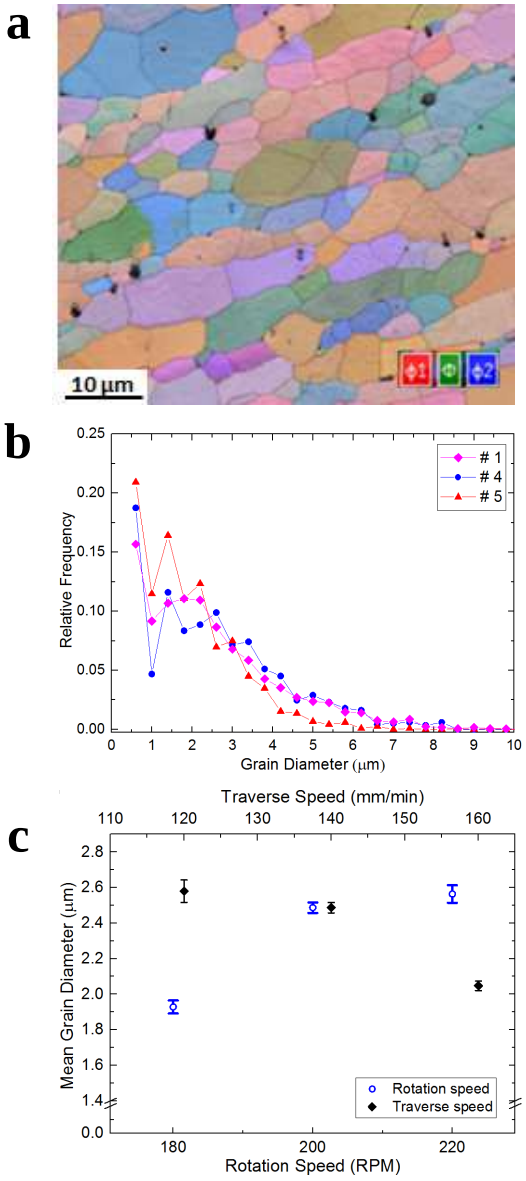
a
10 µm
b
1
4
5
Relative Frequency
Grain Diameter (µm)
c
Traverse Speed (mm/min)
Mean Grain Diameter (µm)
Rotation speed
Traverse speed
Rotation Speed (RPM)

Fig. 3

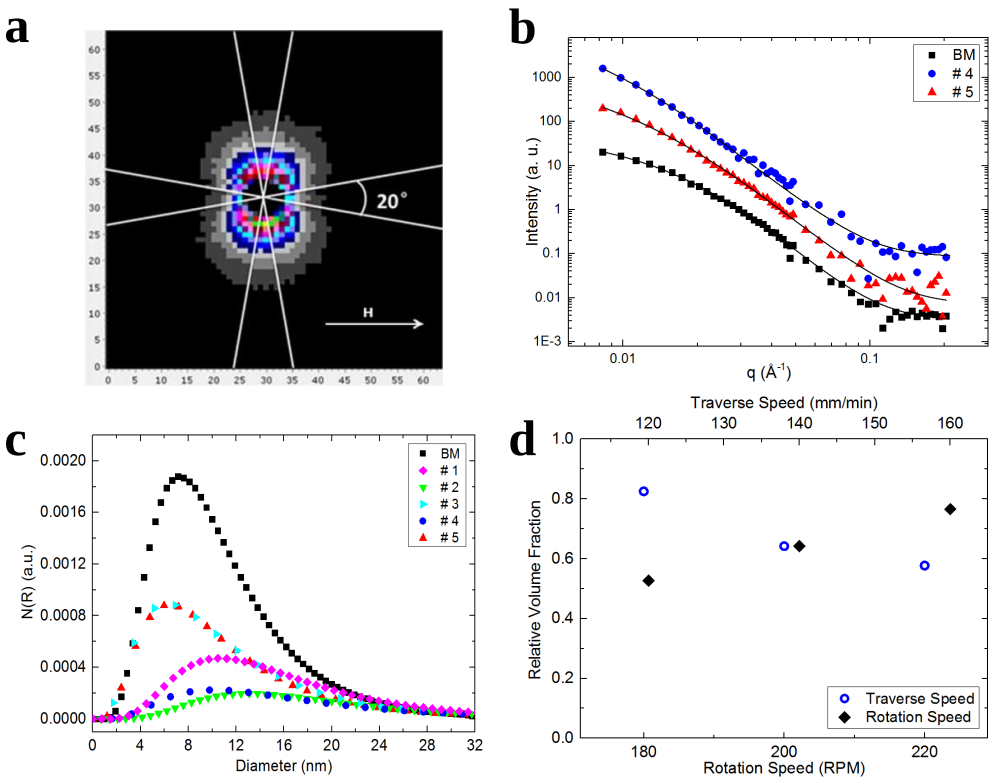
a
20°
H
b
BM
4
5
Intensity (a. u.)
q (Å^{-1})
c
BM
# 1
# 2
# 3
# 4
# 5
N(R) (a.u.)
Diameter (nm)
d
Traverse Speed (mm/min)
Rotation Speed (RPM)
Relative Volume Fraction
Traverse Speed
Rotation Speed

Fig. 4

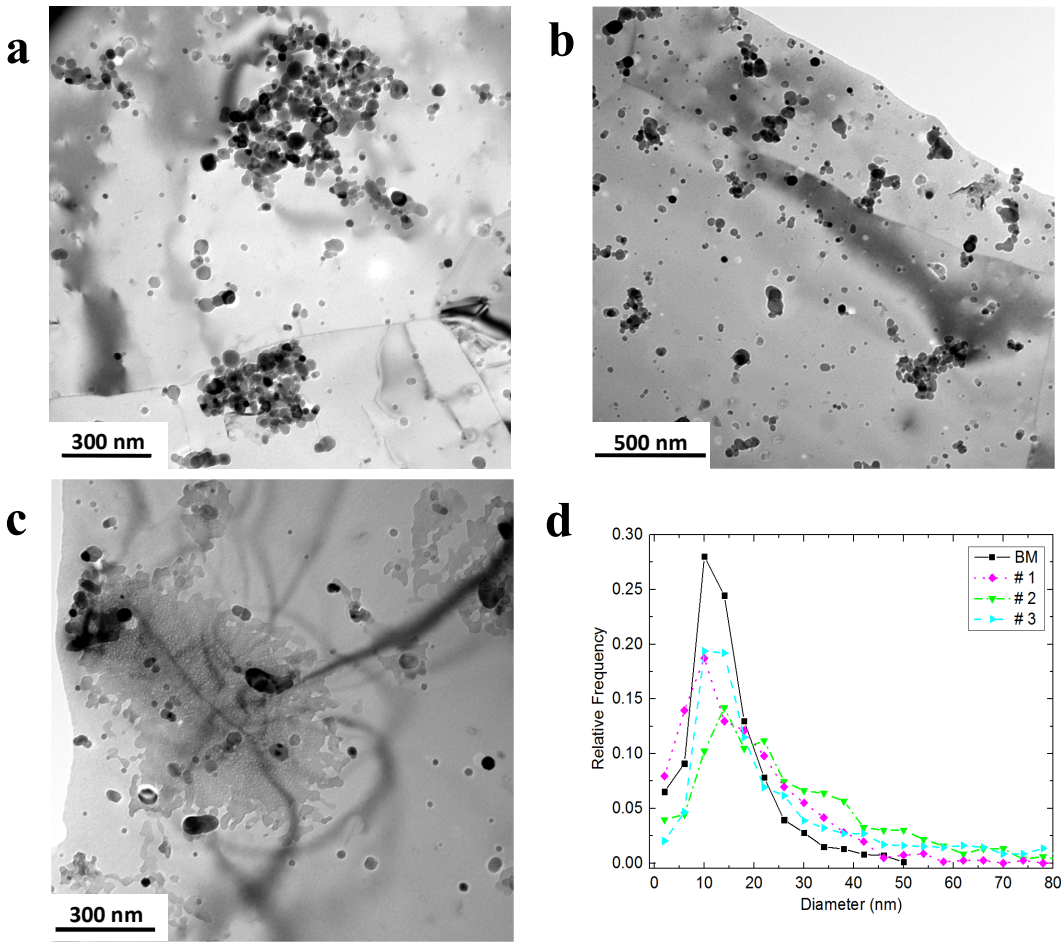
a
300 nm
b
500 nm
c
300 nm
d
BM
1
2
3
Relative Frequency
Diameter (nm)
0.00
0.05
0.10
0.15
0.20
0.25
0.30
0
10
20
30
40
50
60
70
80

Fig. 5

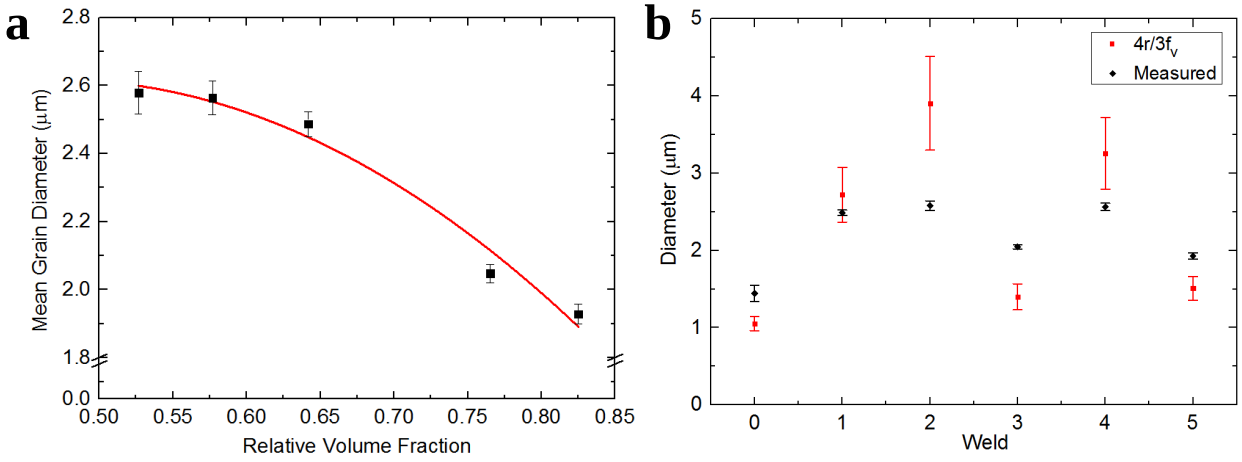
a
Mean Grain Diameter (μm)
Relative Volume Fraction
b
Diameter (μm)
Weld
4r/3f_v
Measured

Fig. 6